NRL Report 7328

Acoustic Near-Field Measurements of a Free-Flooded Magnetostrictive Ring

JOEL A. SINSKY

Transducer Branch
Acoustics Division

December 30, 1971

NAVAL RESEARCH LABORATORY
Washington, D.C.

CONTENTS

ABSTRACT

Precision acoustic near-field pressure magnitude and phase measurements have been made of a radially oscillating free-flooded cylindrical ring. The measurements demonstrate the potential of the NRL Acoustic Research Tank Facility for careful determination of near-field pressure magnitude and phase. Various pressure profiles and phase profiles were plotted. Besides demonstrating results possible with the Tank Facility the profiles were used in deriving dynamic properties of the ring. The transmitting efficiency, surface velocity, and radiation impedance of the ring were derived from the near-field data and were independently confirmed by other methods. Further analysis than that presented here can predict the acoustic interaction through the medium among many rings in an array.

PROBLEM STATUS

This is an interim report on a continuing NRL Problem.

AUTHORIZATION

NRL Problem S02-19
Project RF 05-121-402-6200

Manuscript Submitted July 13, 1971.

ACOUSTIC NEAR-FIELD MEASUREMENTS OF A FREE-FLOODED MAGNETOSTRICTIVE RING

INTRODUCTION

Precision measurements of the acoustic near-field pressure magnitude and phase have been made from a radially oscillating free-flooded cylindrical ring. The measurements were made in the NRL Acoustic Research Tank Facility using pulsed-signal excitation of the transducer and an automatic hydrophone positioning and scanning system. The purpose of these measurements was to demonstrate the near-field capability of the NRL Acoustic Tank, to describe the near field of a radially oscillating free-flooded cylindrical ring, and to derive from the near-field data some dynamic properties of the ring. The near-field radiation pattern of a ring must be known in order to predict the acoustic interaction through the medium among many rings operated in an array configuration.

APPARATUS

The ring transducer used was a wire-wound magnetostrictive permendur core, which was encapsulated in clear Hysol epoxy (Fig. 1). Appendix A gives the details of construction. Figure 2 shows the dimensions of the transducer. Because the epoxy was baked on the wound ring core in a waxed wooden mold, the dimensions of the ring were uniform to 1/64 inch and the surfaces of the transducer were clean and smooth. A simple regular interface between the transducer and the medium, as was achieved with this ring, greatly facilitated mathematical modeling and hence comparison between theory and experiment.

A basic requirement for precision near-field pressure measurements around a transducer is a method to accurately determine the relative position of the hydrophone and the transducer. The necessity to operate the experiment deep enough so the hydrophone would not receive reflected pulses from the surface of the water precluded a conventional optical system for precise determination of the hydrophone position. Instead thin strips of Dynaloy 350 conducting paint, electrically connected to each other and to the metal shaft from which the ring was suspended, were painted on the outside surfaces of the ring (Fig. 1). One end of a small conducting wire was brought up along the hydrophone support shaft out of the water and into a Simpson resistance meter. The other input of the Simpson meter was a wire from the transducer support shaft. When the wire probe adjacent to the hydrophone physically touched one of the painted strips on the transducer, the circuit loop was closed and the electrical resistance of the circuit as measured on the Simpson meter suddenly dropped. Using this method, the location of the hydrophone relative to the transducer was known for a specific configuration of the hydrophone and the transducer to better than 0.05 inch at a depth in the water of 10 feet without recourse to expensive optical techniques. The calibrated

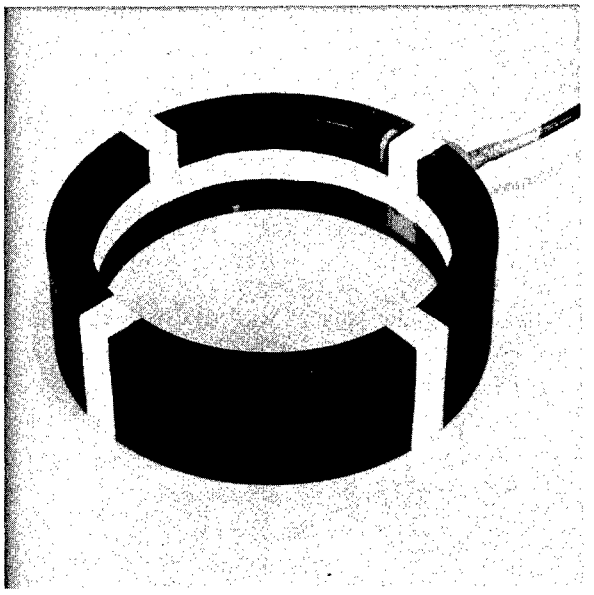

Fig. 1—Transducer

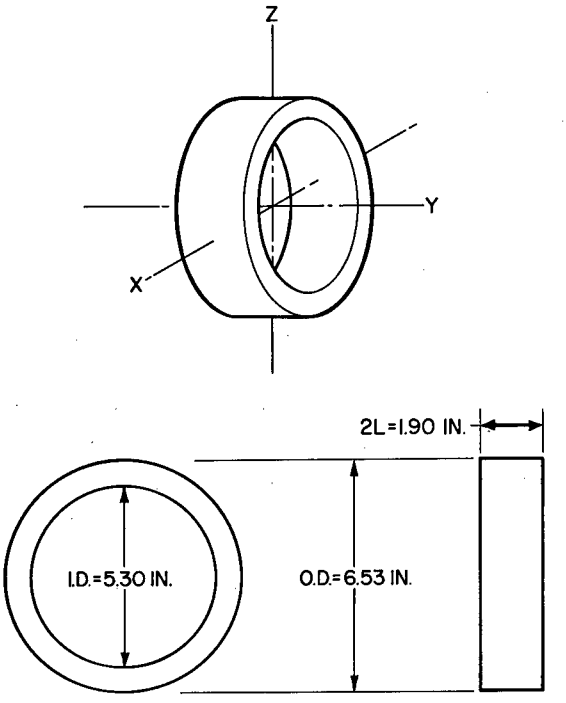

Fig. 2—Dimensions of the Transducer

hydrophone scanning system specified the subsequent locations of the hydrophone relative to its initial position to an accuracy of 0.02 inch over the field of measurements.

The ring was supported in the water by hanging it from a 1/4-inch-diameter bolt which projected from a vertical shaft. The shaft was rotatable and rigidly mounted to a thick metal plate at the top of the tank. Set screws under the plate as well as the rotation of the shaft allowed adjustment of the plane of the ring parallel to the scan plane of the hydrophone. Accelerometers on the ring indicated that its vibration characteristics and velocity distribution were not significantly altered by the method of support. This was corroborated by the degree of symmetry of the near-field pressure scans taken parallel to the plane of the ring.

The block circuit diagrams of the transducer driving system and the receiving system are shown in Fig. 3a and 3b (1). The pulse-modulated driving signal and gated measuring system allowed determination of free-field steady-state data in the confined space of the calibration tank. The voltage across the ring in water during the near-field-scan part of the experiment was 13.8 volts rms, and the current was 0.17 ampere rms.

The hydrophone used in the experiment was an Atlantic Research Model LC-10. The center of the acoustic field was specified as being 0.38 inch back from the tip of the hydrophone and on its axis. Naturally the finite size of the lead zirconate titanate cylindrical sensing element and the hydrophone housing limited the proximity to the transducer at which measurements could be taken. The hydrophone positioning and scanning system enabled either automatic or manual scanning in two directions and manual positioning in the third.

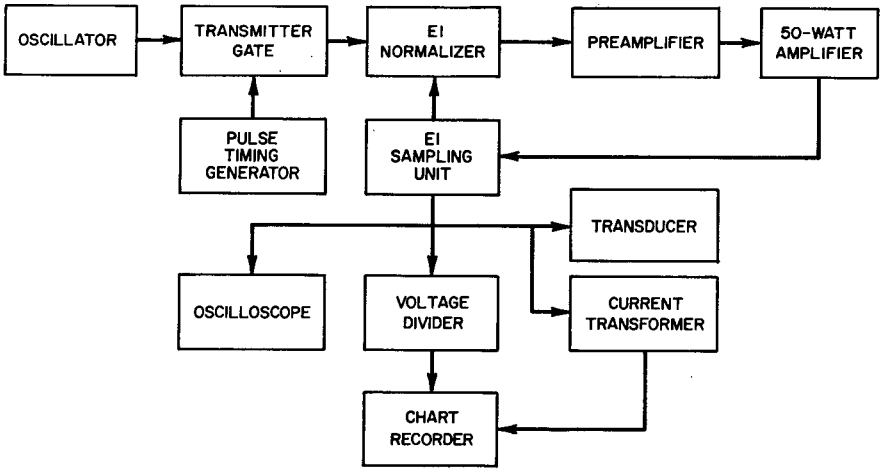

Fig. 3a—Transducer driving system

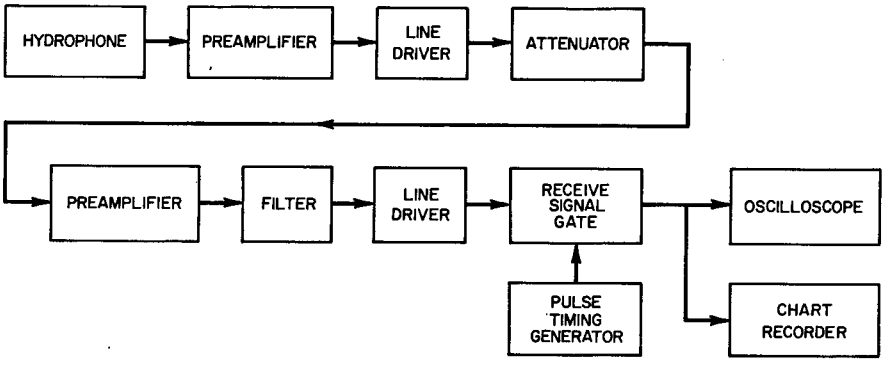

Fig. 3b—Receiving system

The receiving system was calibrated by replacing the hydrophone by an oscillator and a voltmeter. The level of signal was then recorded which produced an arbitrarily chosen level on the chart recorder. 0 dB on the chart record corresponded to a pressure magnitude at the hydrophone acoustic center of 4.0×10^4 microbars, which is designated p_0 in this report.

All pressure phases were measured relative to the driving voltage into the ring. The pressure phase measurements were made by comparing the output of the hydrophone to the driving voltage from the oscillator on an oscilloscope. This method of measuring phase was accurate to ±6 degrees. It was necessary to measure the phase on an oscilloscope because the phasemeters available to the experiment would not accept a pulsed input.

The velocity distribution of the ring was monitored by the use of Endevco 2222B accelerometers. (Appendix B contains a detailed discussion of the accelerometer measurements.) They were fixed directly to the surface of the ring with Eastman 910 epoxy. Because the accelerometers were not watertight, they required a coating which would provide a tight seal in chlorinated water under high-frequency excitation. After extensive testing of commonly used sealants, many of which work in fresh water but leak after prolonged exposure to chlorinated water, a combination Vulcalock and D-202 Gaco vinyl paint was found to be

tight in the environment of the experiment. A primary coat of Vulcalock was applied directly over the accelerometer so that it could eventually be peeled off neatly at the conclusion of the experiment and the accelerometer retrieved intact. The D-202 overcoating provided needed additional protection, because the Vulcalock alone would eventually have leaked. The seals remained good for the 1-week duration of the experiment under conditions of constant immersion and extended pulsing.

EXPERIMENTAL DATA

In air the radial resonant frequency of the ring was 9.4 kHz, the mechanical Q was 151, and the electromechanical coupling coefficient was 0.20. Figure 4 shows a constant-current-drive far-field frequency response of the ring in water for two angular orientations of the ring with respect to the hydrophone. The radial response was taken with the hydrophone on an extended radius of the ring and 3 meters away from the center and the axial response was taken with the hydrophone on the axis of the ring and 3 meters distant from the center. Selected far-field polar plots corresponding to the frequency responses of Fig. 4 appear in Fig. 5. These plots are directivity patterns which are not plotted against the same absolute scale. The recorded pressure level at 0 degrees was arbitrarily adjusted for each plot. Consequently the relative pressure magnitude as a function of angular orientation of the ring at one of the designated frequencies of excitation may be determined from the plots, but the relative pressure magnitude as a function of the frequencies of excitation for a specific angular orientation of the ring may not be determined by a comparison of the plots in Fig. 5. Comparison as a function of frequency is, however, available from Fig. 4 in conjunction with Fig. 5. At 6.1 kHz, where the majority of the near-field scans were taken, the radial response is almost maximum (Fig. 4), and the radial response is nearly flat from approximately 6 kHz to 9 kHz. The axial response over the same frequency range averages 20 dB less and is not as flat over this range. As the single-ring excitation frequency increases beyond 8 kHz, the axial response increases and the radial response decreases. The far-field patterns in Fig. 5 at 9.3 kHz, 9.7 kHz, and 10.3 kHz show this trend. Finally at 12.4 kHz the radial response reaches a minimum (Fig. 4), and the resulting far-field pattern is shown at 12 kHz (Fig. 5). At higher frequencies the response of the ring becomes more intricate, as indicated by the 15-kHz plot.

Figures 6 through 14, to be discussed in the following paragraphs, are results obtained at 6.1 kHz. (All subsequent axis notations will refer to the coordinate system of Fig. 2.) At 6.1 kHz the dimensions of the ring multiplied by the wave number k are

$$ka = 1.91,$$

where a is the mean radius, $k = 2\pi/\lambda$, and $\lambda = 9.74$ inches

$$2Lk = 1.23,$$

where $2L$ is the height of the ring.

The radiated pressure field in a plane perpendicular to the Y axis of a single ring, pulsating in the radial mode with a uniform velocity distribution, is obviously axially symmetric.

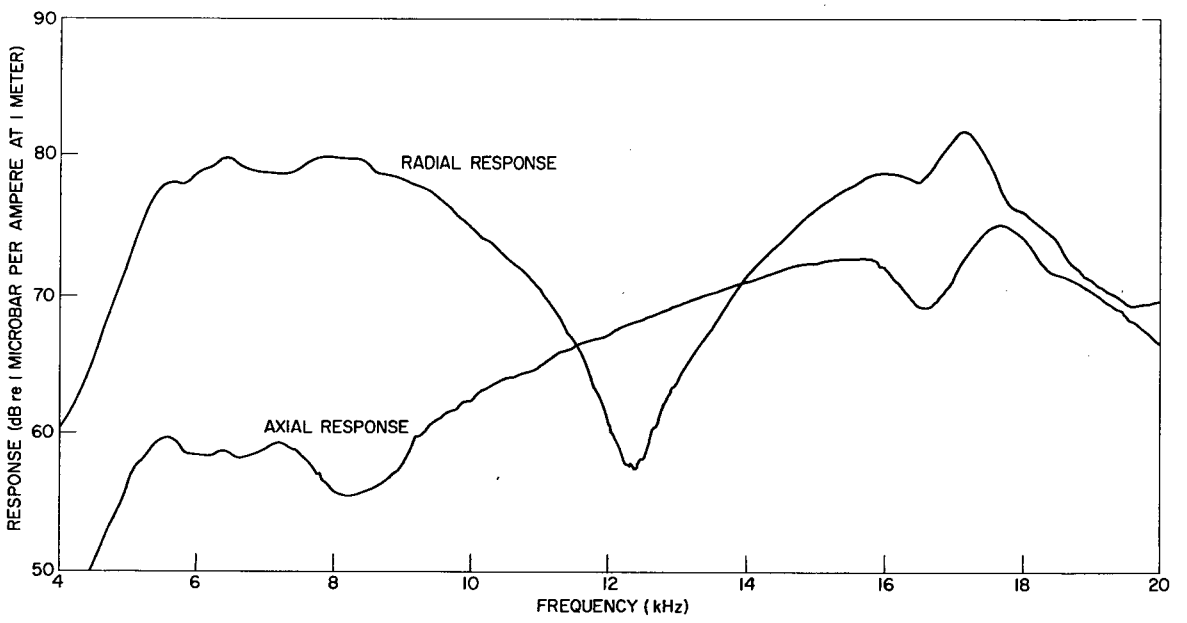

Fig. 4—Far-field transmitting current response of the ring in water

Consequently the pressure isobars anywhere in the field parallel to the plane of the ring and centered on the extended ring axis are concentric circles. Figure 6 shows the measured isobars in a plane perpendicular to the Y axis, the extended axis of the ring, and 0.06λ in front of the ring. The projection of the ring perimeter is superimposed on the scan. The roughly 1/2-dB asymmetry between the top and bottom of the scan is quite likely due to a combination of tilt of the transducer relative to the scan plane of the hydrophone, a slight variation in ring dimensions, and a nonuniform velocity distribution. For a scan taken so near the face of the transducer, variations of the axial velocity of the ring are significant. Figure 6 was made with a typewriter that automatically typed decibel values representing acoustic pressure variations detected by the hydrophone.

Figure 7 shows pressure profiles at varying distances from the front face of the ring. The profiles are not isobars but rather linear scans at fixed distances from and parallel to the front face of the ring. Assuming symmetry, a 360-degree rotation of these pressure profiles gives the pressure everywhere in a 12-inch-diameter cylindrical space in front of and behind the ring.

The detected pressure magnitudes and phases were recorded during the scan as a function of the position of the hydrophone. The pressure profiles in the near field are markedly different from those in the far field, and Fig. 7 clearly shows the beginning of the transition of the ring radiation from its near-field to its far-field structure. Figure 8 shows most of the corresponding pressure phase scans at varying distances from the front face of the ring. The phase across the majority of the ring aperture is nearly constant even in the very near field. As the distance from the ring increases, the variation of the phase decreases as expected, because the ring radiation evolves into spherical waves. Figure 9 is a plot of the pressure magnitude measured along the axis of the ring as a function of Y' the axial distance from the front face of the ring, and Fig. 10 is the corresponding variation in pressure phase. The information exhibited in Figs. 9 and 10 may be derived directly from Figs. 7 and 8.

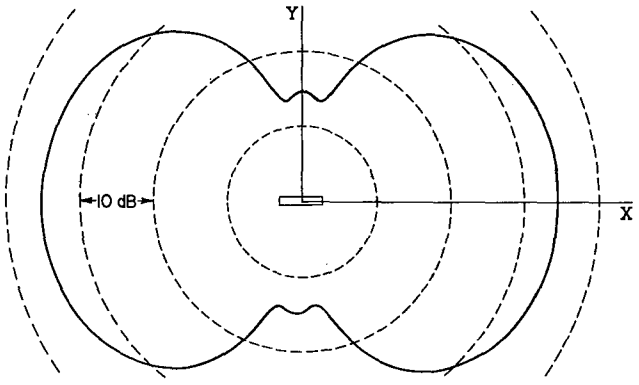

(a) Frequency = 6.1 kHz

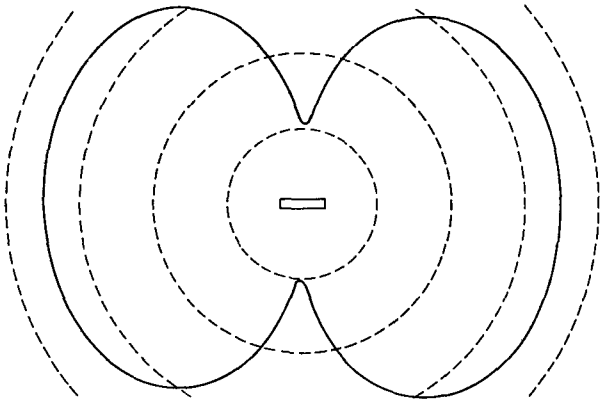

(b) Frequency = 8.0 kHz

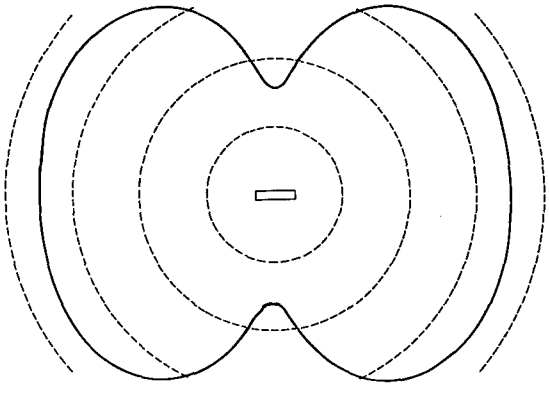

(c) Frequency = 9.3 kHz

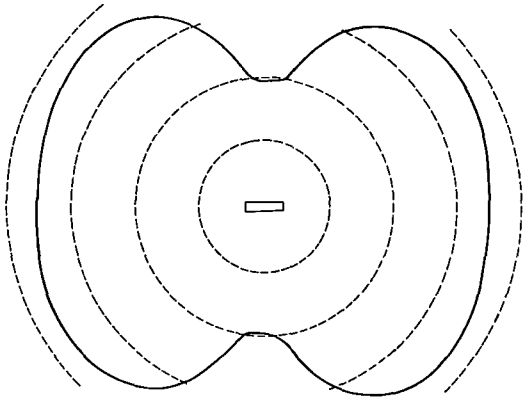

(d) Frequency = 9.7 kHz

(e) Frequency = 10.3 kHz

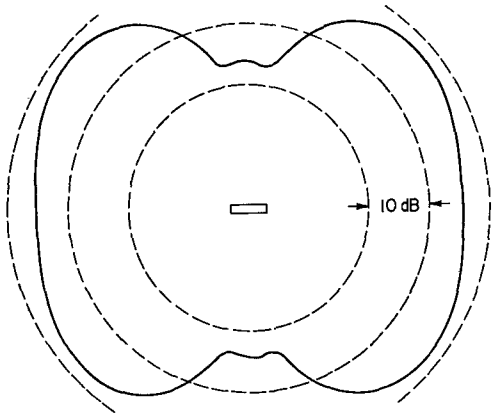

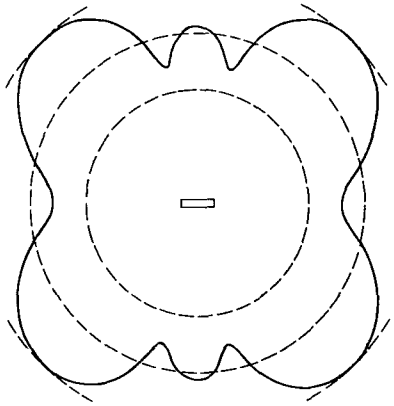

(f) Frequency = 12.0 kHz

(g) Frequency = 15.0 kHz

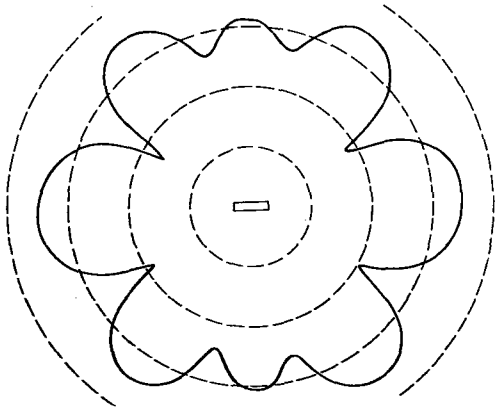

Fig. 5—Far-field polar plots corresponding to the frequency responses of Fig. 4. As shown in Fig. 2, the Z axis is perpendicular to the page. The various plots are not normalized to the same pressure scale; the change in pressure with orientation is 10 dB between adjacent dashed circles in all the plots, but the absolute pressure varies from plot to plot at like circles. Plots for different frequencies can be compared with each other in conjunction with Fig. 4.

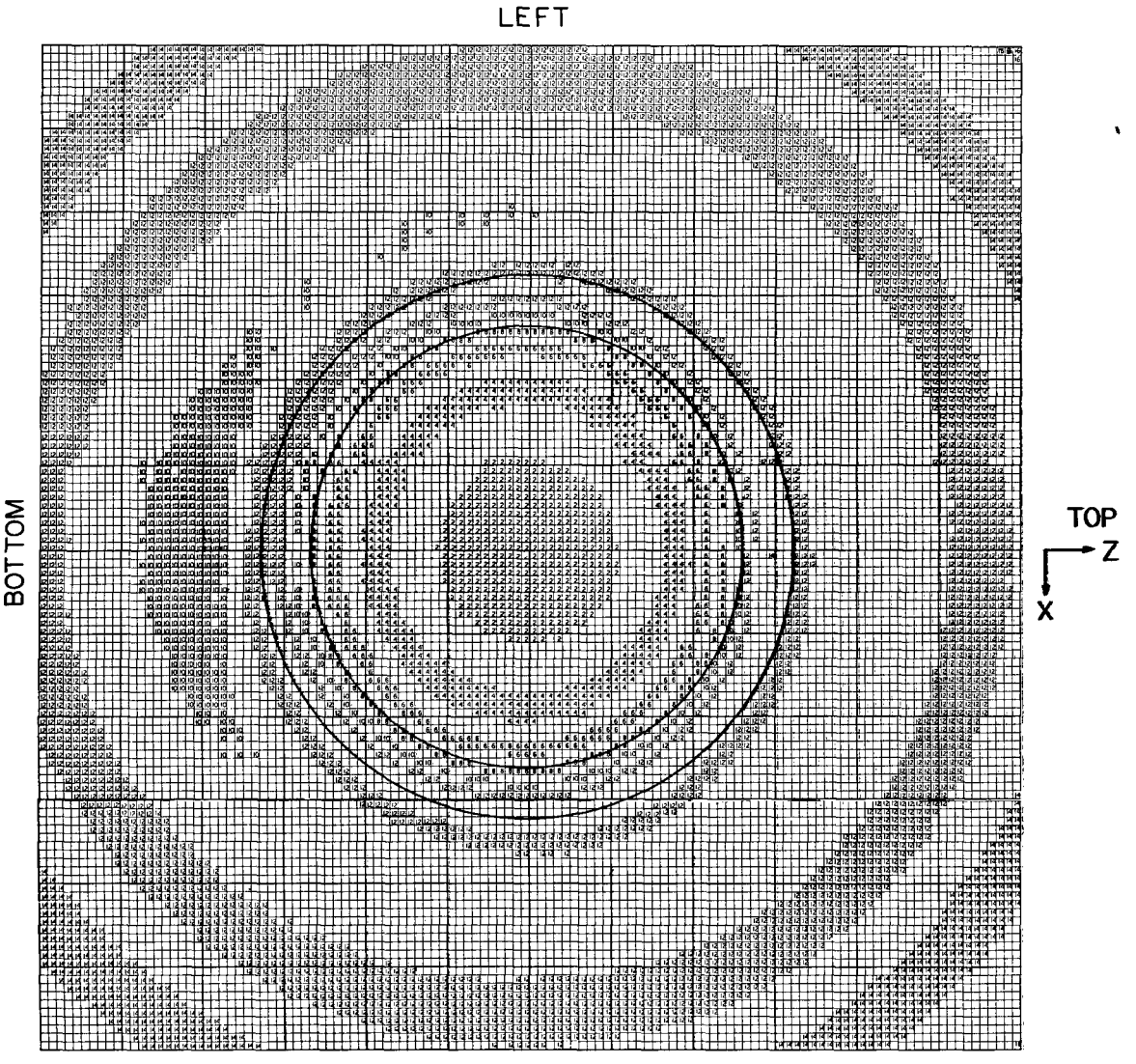

Fig. 6—Pattern at 6.1 kHz taken by an automatic scanner moving a hydrophone in a plane parallel to, and 0.06λ in front of, the front face of the ring. To emphasize the isobars, only the even decibel values were typed.

The near-field measurements shown in Figs. 6 through 10 have been of the axial radiation from the ring. They are indicative of the acoustic coupling that might be expected among elements in a coaxial array. A complete set of pressure magnitude and phase measurements was also taken of the radial radiation, or radiation from the ring along its extended diameter ($Y = 0$). Assuming axial symmetry, one would expect the distance dependence of the radiation along the X axis to be the same as the radiation along the Z axis or any other extended diameter. The experimental evidence of randomly selected extended-diameter scans supports this contention.

Figure 11 displays the phase of the pressure as a function of radial distance inside and outside the ring. The curves of measured phase versus radial distance were extrapolated all the way to the inner and outer surfaces of the ring, and the phase discontinuity across the

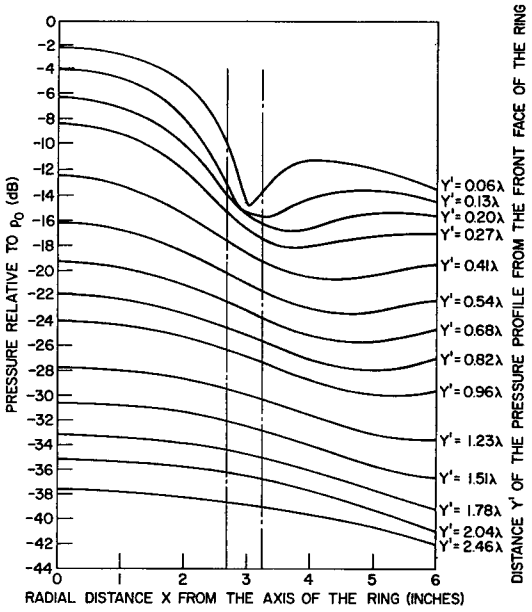

Fig. 7—Pressure profiles at 6.1 kHz at varying axial distances $Y' = Y - L$ from the front face of the ring and up to 6 inches off the axis. Pressure p_0 is 4.0 x 10^4 microbars at the hydrophone acoustic center. The vertical broken lines are projections of the inner and outer surfaces of the ring (Fig. 2).

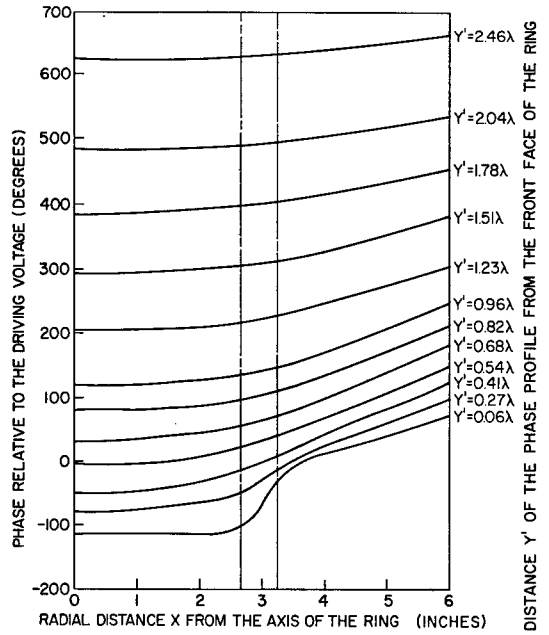

Fig. 8—Profiles of the phase relative to the phase of the ring driving voltage at 6.1 kHz

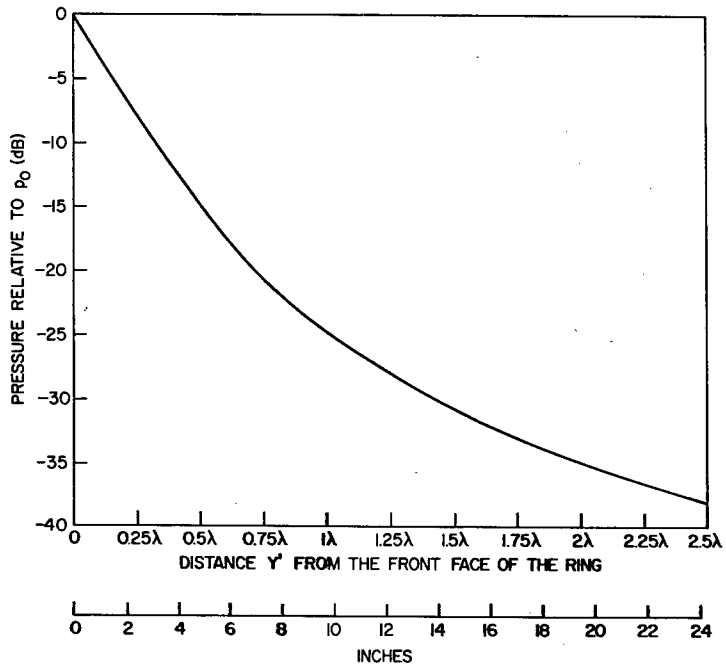

Fig. 9—Profile of the axial pressure at 6.1 kHz as a function of the distance from the front face of the ring

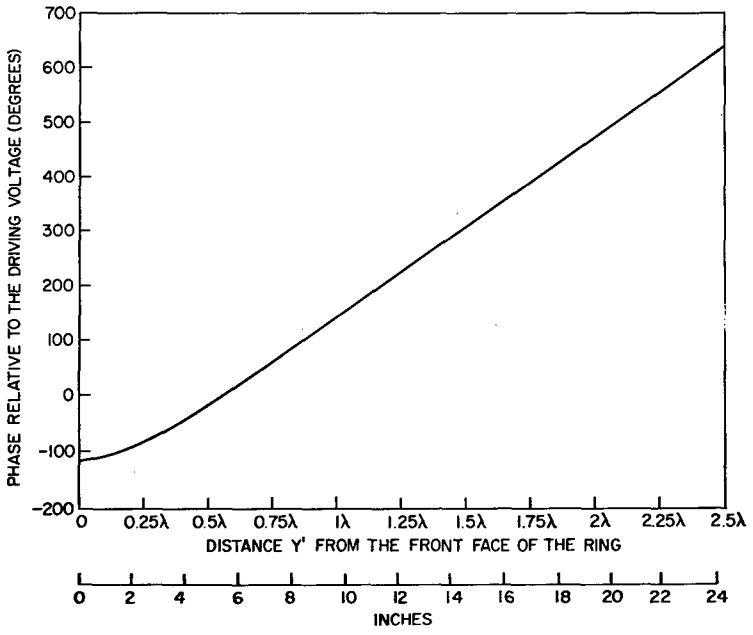

Fig. 10—Profile of the axial phase at 6.1 kHz as a function of the distance from the front face of the ring

thickness of the ring is found to be approximately the expected 180 degrees. The slope of the curve for phase versus radial distance outside the ring is linear beyond 0.25λ and is approximately equal in magnitude to k, the wave number.

Figure 12 is a series of profiles of pressure magnitude versus Y for various values of X', the radial distance from the outside surface of the ring, where $X' = X$ minus the outside radius of the ring. In this figure $Y = 0$ corresponds to an extended diameter of the ring (the X or Z axis) and the vertical broken line at $Y = 0.95$ inch is at the distance L from the X axis. The pressure profiles in the near field rapidly evolve into nearly horizontal lines, or linear isobars parallel to the axis of the ring.

Figure 13 completes the description of the radial near field of the ring by showing the radial pressure as a function of the distance from the outside surface of the ring. Shown are error bars representing the ±0.2 dB uncertainty attached to each data point (first section of Appendix C). The points plotted in Fig. 13 are the values of pressure magnitude on the $Y = 0$ line of Fig. 12. Beyond $X' = 0.25\lambda$ the radial pressure falls off roughly as the inverse of the radial distance from the ring center. Therefore Figs. 11 and 13 indicate that on an extended diameter of the ring for radial distances as little as $X' = 0.25\lambda$ the radiation has the spherical-wave-characteristic amplitude and phase dependence on distance $e^{ik\xi}/\xi$, where ξ is the radial distance from the ring center.

Figure 14 shows one quadrant of an isobaric plot all around the ring in a plane of symmetry which includes a diameter and the axis of the ring. The cylindrical symmetry of the ring permits the curves in the remaining three quadrants to be reproduced by successive mirror images of the one quadrant. Where experimental information is lacking because of large pressure gradients adjacent to the ring's edges, the portions of the isobars in question are drawn

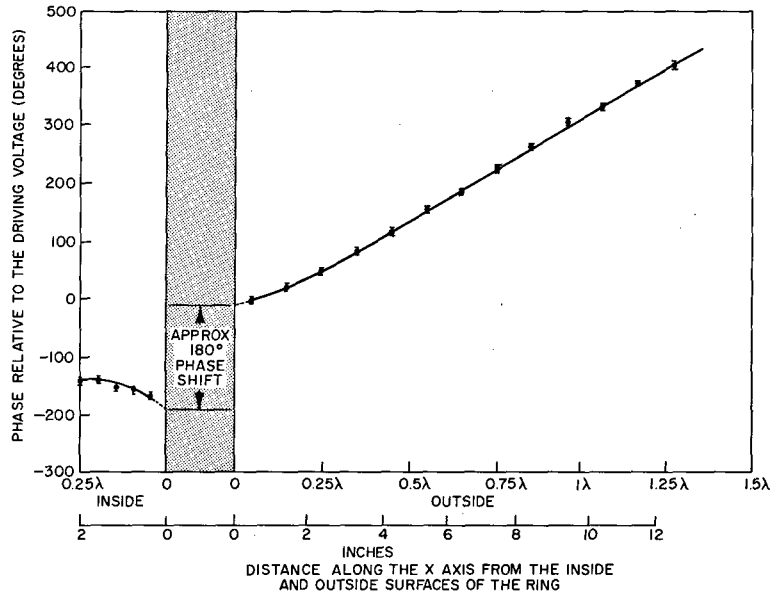

Fig. 11—Profile of the phase relative to the phase of the ring driving voltage at 6.1 kHz in the radial directions from the inside and outside surfaces of the ring. The error bars are ±6 degrees, which was the accuracy of comparing the phases on the oscilloscope.

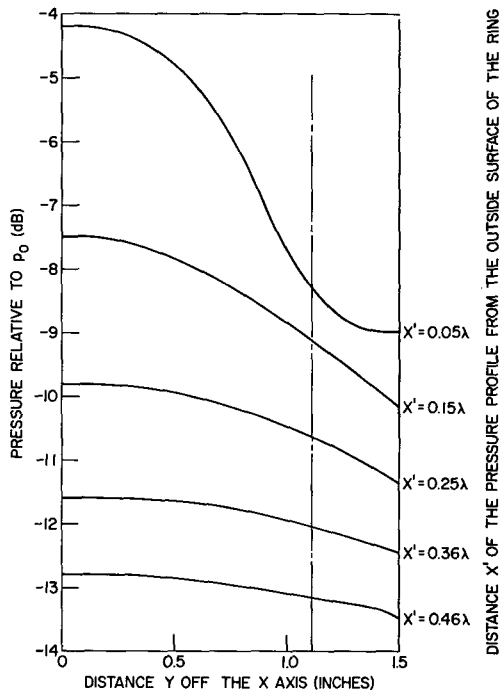

Fig. 12—Pressure profiles at various radial distances from the outside surface of the ring

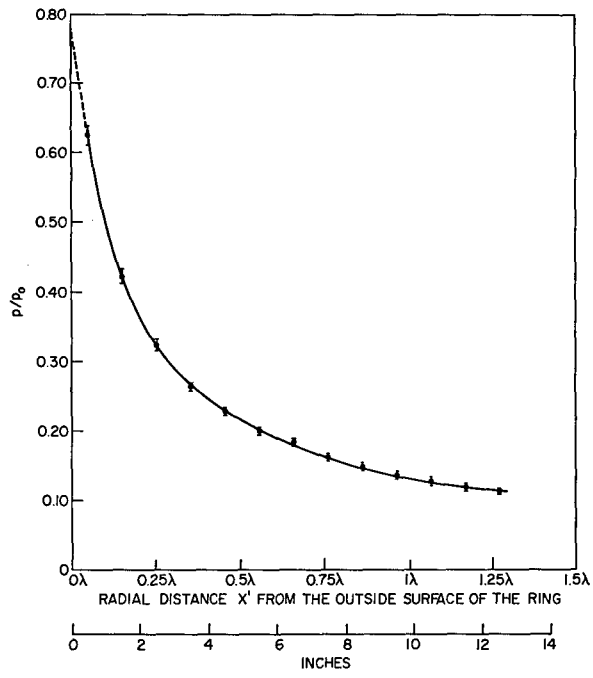

Fig. 13—Profile of the radial pressure at 6.1 kHz as a function of the distance from the outside surface of the ring. The error bars are ±2 dB.

as dashed lines. The maximum pressure in the field of the ring was +0.5 dB, and it was measured at the ring's geometric center. The gradual transition of the form of the radiation pattern from the near to the far field is clearly indicated. The isobar plot reveals at a glance the entire map of pressure magnitude contours.

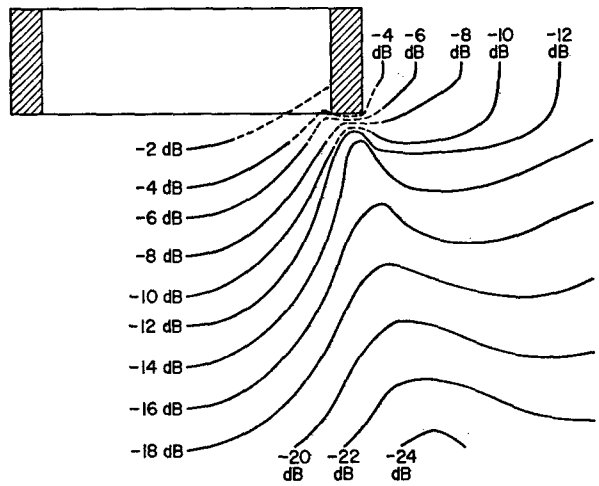

Fig. 14—Pressure isobars. The decibel values refer to the p_0 (4.0×10^4 microbars at the hydrophone acoustic center).

CALCULATION OF TRANSDUCER PARAMETERS

Transmitting Efficiency from Far-Field Data

The transmitting efficiency η of the ring is the ratio of the acoustic power out to the electrical power in (P_a/P_e). If all of the electrical power dissipated in the ring were transformed into radiated acoustic power in the far field, the efficiency of the ring would be 100%. However, input power is also dissipated in various loss mechanisms, such as in the electrical resistance of the ring windings and in the mechanical resistance of the ring core.

From Ref. 2 the expression for the real average acoustic power P_a radiated into the far field is given by

$$P_a = Re \int_S pv^* \, dS, \tag{1}$$

where Re denotes the real part of the integral, S is any closed surface surrounding the source, p is the complex rms pressure (3) evaluated on the increment of surface area dS, and v is the complex conjugate of that component of the complex rms particle velocity which is normal to the increment of surface area dS. Equation (1) can be evaluated in either the near field or the far field. In the far field (4)

$$v^* = \frac{p^*}{\rho c},$$

where ρc is the characteristic impedance of the medium and p^* is the complex conjugate of p. Therefore

$$pv^* = \frac{pp^*}{\rho c} = \frac{|p|^2}{\rho c},$$

where $|p|$ is the absolute value of the complex rms pressure:

$$p = |p|e^{j\alpha},$$

in which α is the phase angle of the complex rms pressure. Consequently in the far field

$$P_a = \mathrm{Re}\int_S \frac{|p|^2}{\rho c}\, dS$$

or

$$P_a = \int_S \frac{|p|^2}{\rho c}\, dS, \tag{2}$$

which is in agreement with Ref. 4. For the far-field frequency response of Fig. 5 the specific electrical drive parameters at 6.1 kHz were

$\mathcal{E}$ = voltage = 16.7 volts rms
I = current = 0.24 ampere rms
Z_e = total electrical impedance = 69.2 ohms
$\cos\beta$ = power factor = 0.15.

The average electrical power dissipated into the ring was

$$\mathcal{E} I \cos\beta = 0.60 \text{ watt}$$

The polar plots of Fig. 5 were generated for a hydrophone-to-transducer separation of 3 meters.

As shown in Fig. 15, r is the vector from the center of the ring to a field point, ϕ is the angle the vector r makes with the Y coordinate axis, and θ is the angle that the projection of the vector r on the XZ plane makes with the X axis. The maximum radial ($\phi = \pi/2$) response at 6.1 kHz was −57.4 dB relative to 1.21 volts, and the sensitivity of the hydrophone was −112.5 dB with respect to 1 volt per microbar. Consequently the pressure detected at $\phi = \pi/2$ (the X axis) in Fig. 5 was 0.69 millibar.

The value of the integral in Eq. (2) was found by a numerical integration of the far-field polar plot at 6.1 kHz shown in Fig. 5a.

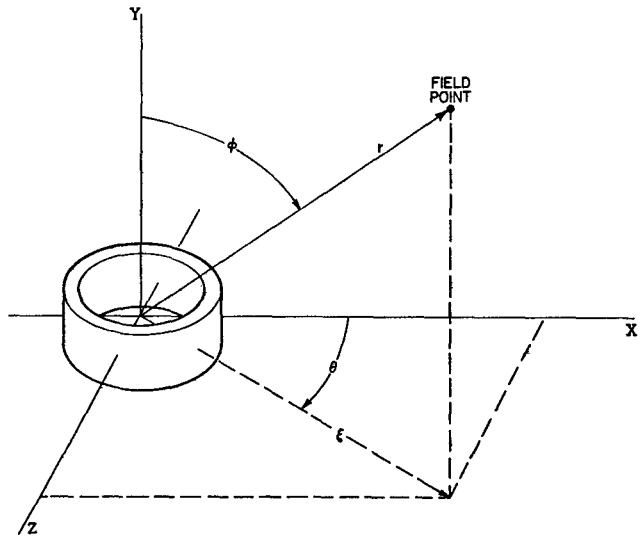

Fig. 15—Spherical coordinates r, ϕ, and θ of a field point. (The radial distance ξ from the ring center is one of the cylindrical coordinates).

An element of surface area with constant radius in spherical coordinates is

$$dS = r^2 \sin\phi \, d\phi d\theta,$$

where $r = |\mathbf{r}|$. The distance r between the hydrophone and the transducer is fixed, since the polar plot was obtained by rotating the transducer about the Z, or $\theta = \pi/2$, axis while the hydrophone position on the Y, or $\phi = 0$, axis remained unchanged. Thus

$$\int |p|^2 dS = \int_0^{2\pi} \int_0^{\pi} |p(\phi)|^2 r^2 \sin\phi \, d\phi d\theta = 2\pi r^2 \int_0^{\pi} |p(\phi)|^2 \sin\phi \, d\phi.$$

The pressure is a function of only ϕ and, in fact, exhibits symmetry about the Z, or $\theta = \pi/2$ axis. Consequently, using

$$\int |p|^2 dS = 4\pi r^2 \int_0^{\pi/2} |p(\phi)|^2 \sin\phi \, d\phi,$$

$$\left| p\left(\phi = \frac{\pi}{2} \text{ radians}\right) \right| = 0.69 \text{ millibar},$$

$$r = 300 \text{ cm},$$

and

$$\rho c = 15 \times 10^4 \text{ g/cm}^2 \text{ sec},$$

the numerical integration by Eq. (2) yielded $P_a = 0.22$ watt. The transmitting efficiency is

$$\eta = \frac{P_a}{P_e} \times 100\% = \frac{0.22}{0.60} \times 100\% = 37\%.$$

(The directivity factor and the directivity index can also be calculated. The directivity factor R of the ring at 6.1 kHz is given by

$$R = \frac{4\pi r^2 \left| p\left(\phi = \frac{\pi}{2}\right) \right|^2}{\int |p|^2 dS} = 1.7 .$$

The directivity index D_i of the ring is $D_i = 10 \log_{10} R = 10 \log_{10} 1.7 = 2.3$ dB.)

Radial Surface Velocity From Near-Field Data

The simplest and most accurate method to calculate the acoustic efficiency and directivity index of a transducer from experimental data was that of the preceding subsection using the far-field response characteristics of the transducer. However, because of limitations in the size of acoustic tank facilities relative to the size of a transducer, it is not always possible to measure the pressure magnitude in the far field of the transducer. Then near-field pressure-magnitude and phase data along with a complete profile of the transducer's velocity magnitude and phase can be used for the calculation of efficiency.

The near-field scans of Figs. 6 through 14 were done for different voltage and current into the ring than the value of ring drive for the far-field responses previously considered. For the near-field scans the average electrical power P_e dissipated into the ring was 0.35 watt rather than 0.60 watt dissipated for the far-field responses. All of the measurements of pressure magnitude were referred to $p_0 = 4.0 \times 10^4$ microbars rms, which corresponded to 0 dB on the chart recorder. The maximum pressure measured in the field of the ring was at the geometric center of the ring and was +0.5 dB, or 4.2×10^4 microbars rms.

Let the scalar velocity potential in the radiation field of the transducer be

$$\tilde{\psi}(\theta, \xi, y, t) = \sqrt{2}\, \psi(\theta, \xi, y) e^{-jwt},$$

where

$\tilde{\psi}$ = time-dependent scalar velocity potential,
ψ = complex rms value of the scalar velocity potential,
w = 2π x frequency = $2\pi \times 6100\ \text{sec}^{-1}$,
ξ = the component of r in the XZ plane (since ξ is also directed along the radius of the ring, it is designated the ring radial coordinate),
θ = the angle that ξ makes with the X axis,
y = the Y component of r.

Thus θ, ξ, and y are the cylindrical coordinates locating a field point (Fig. 15).

The time-dependent particle velocity in the medium is given by

$$\tilde{\mathbf{v}} = -\nabla\tilde{\psi}.$$

The ring radial component of the particle velocity is

$$\tilde{v}_\xi = -\frac{d\tilde{\psi}}{d\xi}$$

The time-dependent acoustic pressure and velocity potential are related by

$$\tilde{p} = \rho\frac{d\tilde{\psi}}{dt} = -jw\rho\tilde{\psi}$$

or

$$\tilde{\psi} = \frac{\tilde{p}}{-jw\rho},$$

where ρ is the density of the medium. Substituting this expression for $\tilde{\psi}$ into the equation for the ring radial component of the particle velocity, an expression is derived relating the ring radial component of the particle velocity and the pressure:

$$\tilde{v}_\xi = \frac{1}{jw\rho}\frac{d\tilde{p}}{d\xi}.$$

The complex rms ring radial component of the velocity and complex rms pressure are similarly related:

$$v_\xi = \frac{1}{jw\rho}\frac{dp}{d\xi}.$$

The complex rms pressure anywhere in the field has magnitude and phase

$$p = |p|e^{j\alpha}.$$

Both the magnitude and phase of p depend on ξ. Thus

$$v_\xi = \frac{1}{jw\rho}\left(\frac{d|p|}{d\xi}e^{j\alpha} + j|p|e^{j\alpha}\frac{d\alpha}{d\xi}\right). \tag{3}$$

The magnitude of $v_\xi = |v_\xi|$:

$$|v_\xi| = \sqrt{v_\xi v_\xi^*} = \frac{1}{w\rho}\left[\left(\frac{d|p|}{d\xi}\right)^2 + \left(|p|\frac{d\alpha}{d\xi}\right)^2\right]^{1/2}. \tag{4}$$

The ring radial component of the particle velocity is continuous across the boundaries of the transducer. Therefore, an evaluation of $|v_\xi|$ at the inner and outer radially oscillating surfaces

of the ring is equivalent to calculating the ring radial component of the velocity of these surfaces. (With reference to Figs. 2 and 15 the inner surface of the ring is where ξ = I.D./2 and the outer surface is where ξ = O.D./2.)

Accelerometer measurements (Appendix B) have established that, at 6.1-kHz radial excitation of the ring, the inside and outside ξ components of the ring velocity differ in phase by 180 degrees. Furthermore, within the measurement accuracy of the accelerometers, the velocity of the ring surfaces is found to be axially uniform and the magnitude of the inside surface radial velocity of the ring is equal to the magnitude of the outside surface radial velocity. Therefore the ring radial component of the surface velocity need be calculated at only one point to know it everywhere. The point chosen for this calculation is a point on the outside surface of the ring along the circumferential line that bisects the ring. In terms of coordinates the point is at $y = 0$ and ξ = the outside radius of the ring. Parameters evaluated at this point are designated by the subscript c.

From the profile in Fig. 11 extrapolated to the surface of the ring

$$\left(\frac{\Delta\alpha}{\Delta\xi}\right)_c = 8\,\frac{\text{degrees}}{\text{cm}} = 0.14\,\frac{\text{radian}}{\text{cm}} .$$

From Fig. 13

$$\left(\frac{\Delta|p|}{\Delta\xi}\right)_c = -0.50 \times 10^4\,\frac{\text{dynes}}{\text{cm}^3}$$

and

$$|p|_c = 0.78 p_0 = 3.1 \times 10^4\,\frac{\text{dynes}}{\text{cm}^2} .$$

$(\Delta|p|/\Delta\xi)_c$ is negative because pressure magnitude decreases as the radial distance from the ring increases.

Substituting these measured values along with $\rho = 1$ g/cm^3 into Eq. (4),

$$|v_\xi|_c = \frac{1}{2\pi \times 6100 \times 1}\left[(0.50)^2 + (3.1 \times 0.14)^2\right]^{1/2} \times 10^4 \qquad (5)$$

$$= 0.17 \text{ cm/sec rms.}$$

The magnitude of the ring's radial velocity determined from accelerometer measurements was 0.15 cm/sec rms (Appendix B). Thus the velocity of the ring derived from near-field pressure data agrees with that measured directly by accelerometers to within 15%.

Transmitting Efficiency From Near-Field Data

As stated earlier, the transmitting efficiency of the transducer is $\eta = (P_a/P_e) \times 100\%$, where P_a is the real average acoustic power radiated into the far field and P_e is the electrical power into the ring. Equation (1) for P_a does not have to be restricted to the far field however; it can be evaluated over any closed surface surrounding the source, even a surface at the source boundaries. The measured pressure magnitude and phase varies along the height of the ring (as a function of y). Therefore, the P_a integral was replaced by a sum over circumferential strips, and values of pressure magnitude and phase were measured to correspond to each strip. Each strip was 1/12 inch wide; hence the magnitude and phase of the pressure were measured every 1/12 inch along the height of the ring. Since the ring is 1.90 inches high, 23 strips were included in the summation for each surface of the ring, making a total of 46 strips for the entire P_a integral. It is shown in Appendix C (in the section "Edge Radiation") that the contributions to the integral from the ring's edges at $y = +L$ and $y = -L$ are negligible.

The complex conjugate of the complex rms ring radial velocity from Eq. (3) is

$$v_\xi^* = -\frac{1}{jw\rho}\left(\frac{d|p|}{d\xi}e^{-j\alpha} - j|p|e^{-j\alpha}\frac{d\alpha}{d\xi}\right)$$

$$= -\frac{1}{jw\rho}\left(\frac{d|p|}{d\xi} - j|p|\frac{d\alpha}{d\xi}\right)e^{-j\alpha},$$

where $p = |p|e^{j\alpha}$. Let α_c, $|p|_c$, $(d\alpha/d\xi)_c$, and $(d|p|/d\xi)_c$ be respectively the pressure phase, magnitude, phase gradient, and magnitude gradient measured at ξ = outside radius and $y = 0$. The magnitude and phase of v_ξ, the ring radial component of the ring's surface velocity, is assumed constant along the height of the ring, both in magnitude and in phase. Therefore,

$$v_\xi^* = -\frac{1}{jw\rho}\left[\left(\frac{d|p|}{d\xi}\right)_c - j|p|_c\left(\frac{d\alpha}{d\xi}\right)_c\right]e^{-j\alpha_c}$$

for all of the circumferential strips on the outside of the ring. For the circumferential strips on the inside of the ring $\alpha = \alpha_c - \pi$, so that

$$v_\xi^* = -\frac{1}{jw\rho}\left[\left(\frac{d|p|}{d\xi}\right)_c - j|p|_c\left(\frac{d\alpha}{d\xi}\right)_c\right]e^{-j(\alpha_c-\pi)}.$$

The notation used is $\alpha_i = \alpha_c + \epsilon_i$ for the pressure phase measured relative to the ring driving voltage for the ith circumferential strip and $|p|_i$ for the corresponding rms amplitude.

Expressing Eq. (1) as a summation over 46 strips:

$$P_a = \mathrm{Re}\left(\underbrace{\sum_{i=1}^{23} p_i v_\xi^* \Delta S_i}_{\substack{\text{(outside-}\\ \text{surface}\\ \text{strips)}}} + \underbrace{\sum_{i=24}^{46} p_i v_\xi^* \Delta S_i}_{\substack{\text{(inside-}\\ \text{surface}\\ \text{strips)}}}\right), \tag{6}$$

where

$$p_i = |p|_i e^{j\alpha_i} = |p|_i e^{j(\alpha_c+\epsilon_i)}.$$

For the outside surface

$$\Delta S_i = \pi \text{ x outside diameter x strip width}$$

$$= \frac{\pi}{12} \text{ x } 6.53 \text{ x } 2.54^2 \text{cm}^2.$$

For the inside surface

$$\Delta S_i = \pi \text{ x inside diameter x strip width}$$

$$= \frac{\pi}{12} \text{ x } 5.30 \text{ x } 2.54^2 \text{cm}^2.$$

For the outside surface

$$\begin{aligned}\mathrm{Re}(p_i v_\xi^*) &= \mathrm{Re}\left\{|p|_i e^{j(\alpha_c+\epsilon_i)}\left(-\frac{1}{j\omega\rho}\right)\left[\left(\frac{d|p|}{d\xi}\right)_c - j|p|_c\left(\frac{d\alpha}{d\xi}\right)_c\right]e^{-j\alpha_c}\right\} \\ &= \mathrm{Re}\left\{|p|_i \frac{e^{j\epsilon_i}}{w\rho}\left[j\left(\frac{d|p|}{d\xi}\right)_c + |p|_c\left(\frac{d\alpha}{d\xi}\right)_c\right]\right\} \\ &= \frac{|p|_i}{w\rho}\left[|p|_c\left(\frac{d\alpha}{d\xi}\right)_c \cos\epsilon_i - \left(\frac{d|p|}{d\xi}\right)_c \sin\epsilon_i\right].\end{aligned}$$

Similarly for the inside surface

$$\mathrm{Re}(p_i v_\xi^*) = \frac{-|p|_i}{w\rho}\left[|p|_c\left(\frac{d\alpha}{d\xi}\right)_c \cos\epsilon_i - \left(\frac{d|p|}{d\xi}\right)_c \sin\epsilon_i\right].$$

Substituting in Eq. (6),

$$P_a = \frac{1}{w\rho}\left\{\sum_{\substack{i=1 \\ \text{(outside)}}}^{23} |p|_i\left[|p|_c\left(\frac{d\alpha}{d\xi}\right)_c \cos\epsilon_i - \left(\frac{d|p|}{d\xi}\right)_c \sin\epsilon_i\right]\Delta S_i\right.$$

$$\left. - \sum_{\substack{i=24 \\ \text{(inside)}}}^{46} |p|_i\left[|p|_c\left(\frac{d\alpha}{d\xi}\right)_c \cos\epsilon_i - \left(\frac{d|p|}{d\xi}\right)_c \sin\epsilon_i\right]\Delta S_i\right\}. \qquad (7)$$

A tabulation of the $|p|_i$'s and ϵ_i's is given in Appendix D as well as the resulting numerical calculation of P_a:

$$P_a = 0.15 \text{ watt.}$$

As was stated, the real electrical power dissipated into the ring for the near-field scans is $P_e = 0.35$ watt. Therefore the transmitting efficiency calculated entirely from the near field is

$$\eta = \frac{0.15}{0.35} \times 100\% = 43\%.$$

The transmitting efficiency calculated from the far-field data was 37%, resulting in a difference between the two calculations of $43\% - 37\% = 6\%$.

Radiation Impedance

The radiation impedance Z of the ring is an important parameter which can be determined from only the near-field data and, from Ref. 5, is

$$Z = \frac{\int_S p v_\xi^* \, dS}{v v^*}, \tag{8}$$

where p is the complex rms pressure at the increment of surface area dS of the source, v_ξ^* is the complex conjugate of the complex rms normal velocity of the source at the increment of surface area dS, and v is a reference velocity; (The reference velocity v might, for example, be the average normal velocity, or any other nonzero value of the normal velocity which is convenient for a particular purpose. Z is then termed the radiation impedance referred to the velocity v.) For this calculation v is chosen to be the rms value of the ring's radial velocity whose magnitude was calculated in Eq. (5); hence

$$v v^* = |v|^2 = (0.17)^2 = 0.029(\text{cm/sec})^2.$$

In terms of summations over strips

$$\int p v_\xi^* \, dS = \underbrace{\sum_{i=1}^{23} p_i v_\xi^* \, \Delta S_i}_{\text{(outside)}} + \underbrace{\sum_{i=24}^{46} p_i v_\xi^* \, \Delta S_i}_{\text{(inside)}}.$$

The above summations are the same as those found in Eq. (6). They are evaluated in Appendix D and yield the result

$$\int_S p v_\xi^* \, dS = (15 - 17j) \times 10^5 \text{ dyne cm/sec.}$$

Therefore $Z = (52 - 59j) \times 10^6$ dyne sec/cm.

A computer program (SHIP) has been written and tested by Rogers (6) at NRL which predicts beam patterns, surface pressures, and radiation impedance for a ring source when the velocity distribution is known. For the ring used in this experiment and neglecting edge radiation, SHIP predicted a radiation impedance of

$$Z_{\text{SHIP}} = (44 - 57j) \times 10^6 \text{ dyne sec/cm.}$$

The percent deviations of the real and imaginary parts of Z between the experimental and the analytical results are:

$$\text{deviation in Re } Z = 18\%,$$

$$\text{deviation in Im } Z = 3.5\%.$$

CONCLUSIONS

In this report the near-field pressure contours of a free-flooded ring excited in its radial mode have been documented, and the potential of the NRL Research Tank Facility for precision underwater sound measurements has been indicated. All of the recorded data relevant to the experiment have not been presented here, nor has all of the analysis performed using the data been described. Rather, representative samples of the data which were thought to be of most interest to researchers in the field were selected for presentation. The analysis presented includes only sample calculations which serve to demonstrate the variety of information which can be gleaned from near-field measurements. Improvements are being implemented or sought in the experimental facilities at NRL, particularly in more accurate measurement of the velocity of a transducer, greater resolution of the pressure magnitude and phase in the radiation field by the use of a smaller hydrophone and a larger transducer, and more accurate alignment techniques. At present, however, the facilities are adequate and available to provide much useful information for the underwater acoustic theorist.

ACKNOWLEDGMENTS

The author is grateful for many valuable discussions with J. Munson, S. Hanish, L. Van Buren, R. Baier, J. Trott and P. Rogers. Appreciation is expressed for assistance in the preparation of the transducer to D. Gregan and D. Dorsey and for assistance in taking the measurements to J. Neeley.

REFERENCES

1. J. Chervenak, "A New NRL Acoustic Research Tank Facility," NRL Report 6822 (1969).
2. L.L. Foldy, "Theory of Passive Linear Electroacoustic Transducers with Fixed Velocity Distribution," J. Acoust. Soc. Amer. 21, 595 (1949).

3. E.R. Peck, "Electricity and Magnetism," New York, McGraw-Hill (1953), pp. 379 and 392.
4. L. Camp, "Underwater Acoustics," New York, Wiley-Interscience (1970), p. 178.
5. C.H. Sherman, "Mutual Radiation Impedance of Fixed Velocity Distribution Transducers," USL Technical Memorandum 912-1-74-61 (1961).
6. P. Rogers, "SHIP—A Fast Computer Program for Calculating the Acoustic Radiation and Radiation Impedance for Free Flooded Ring and Finite Circular Cylinder Sources," NRL Report 7240 (1971)

APPENDIX A
CONSTRUCTION DETAILS OF THE TRANSDUCER

THE RING CORE

The core material of the magnetostrictive ring transducer used in this experiment was 2*V* permendur. It was scroll wound, which means that it was made by winding a metal strip about a mandrel and using a bonding agent to hold it permanently. The strip was 0.007 inch thick, and the finished core dimensions were: outside diameter, 6.13 inches; inside diameter, 5.63 inches; height, 1.50 inches; and weight, 1.86 pounds. The core was then wound with linen tape to insulate it from 210 turns of No. 19 wire wound directly over the tape. The resulting toroidally wound permendur scroll core was polarized by briefly passing 70 amperes dc through the windings. The electrical impedance of the core assembly was measured in air as a function of frequency for low-power drive, and the following dynamic parameters were derived from the measurement: Q_m = the figure of merit = 56, radial resonant frequency = 11,331 Hz, and k = electromechanical coupling coefficient = 0.18.

THE ENCAPSULATED RING TRANSDUCER

The ring core was encapsulated in clear Hysol epoxy. A waxed wooden mold was fabricated to house the ring core while the Hysol epoxy was poured around it. The inside dimensions of the mold corresponded to the desired finished dimensions of the transducer. Precautions were taken before, during, and after the epoxy was poured in order to insure that it was free of trapped air. The mold was placed in an oven and baked at 60°C for 4 hours—ample time for the epoxy to harden. The resulting encapsulated transducer was then removed from the wooden mold, cleaned, and sanded.

The finished dimensions of the ring are shown in Fig. 2, and the corresponding weight was 2.93 pounds. The electrical impedance of the ring transducer was measured in air as a function of frequency for low power drive and the dynamic parameters measured were: Q_m = 151, radial resonant frequency = 9353 Hz, and k = electromechanical coupling coefficient = 0.20. The permeability of the ring was 66.

Measurements in water of the pressure magnitude and phase of the ring radiation as well as the electrical impedance of the ring were repeatable only when the ring was allowed to soak for approximately 24 hours after it was first put in the water. This was probably due to the slow absorption of water by the Hysol potting material.

APPENDIX B
ACCELEROMETER MEASUREMENTS

The accelerometers used in this experiment were Endevco model 2222B, which are self-generating shear-type piezoelectric transducers requiring no external power for operation. Since each accelerometer weighed only 0.5 gram and had maximum dimensions 0.250 inch wide, 0.375 inch long, and 0.125 inch high, the accelerometers monitoring the transducer motion did not load the transducer. The accelerometers were epoxied to the surface of the ring, and the output of the accelerometers was fed directly into an Endevco model 2713 laboratory charge amplifier. The charge-amplifier output was fed to both a digital voltmeter and an oscilloscope. The voltages read on the digital voltmeter were directly proportional to the acceleration amplitude and hence to velocity amplitude. The phase of the acceleration was compared to a reference signal on the oscilloscope.

As a result of numerous accelerometer readings it was concluded that the velocity distribution of the ring transducer was circumferentially uniform, that the inside surface radial velocity was very nearly equal to the outside surface radial velocity, and that the axial velocity was approximately 15% of the radial velocity. A uniform circumferential velocity distribution is one where the inside and the outside surface velocities of the ring are independent of θ (Fig. 15). The axial velocity of the ring is the surface velocity directed along the Y coordinate axis. It is therefore the velocity of the ring's edges (the surfaces at $y = \pm L$).

Most of the accelerometer measurements on the ring were done in air, and the results of these measurements were then checked at a few points on the ring in water. The reasons for this procedure were the considerable coating precautions required to insure watertight integrity and the resultant inconvenience of moving the available accelerometers about underwater to many different locations on the transducer to gather the necessary statistics from a large number of readings. Six accelerometers were used to make 12 determinations (two determinations per accelerometer) in air of the outside surface velocity and of the inside surface velocity and six determinations of the axial velocity. The accelerometers were uniformly spaced about the circumference of the ring, and the ring was excited at 6.1 kHz with a current of 150 milliamperes rms. Furthermore, the ring was suspended from a single cantilevered ¼-inch-diameter bolt just as it was in water. The rms recorded voltages E which were proportional to the measured velocities appear in Table B1. The variation of the readings was most likely due to the nonuniformity of the Eastman 910 epoxy joints between the accelerometers and the ring surface. After an accelerometer was epoxied to the ring, its output voltage was repeatable for consecutive excitations of the ring at constant current and linearly proportional to the magnitude of the excitation current. Moreover 12 consecutive applications of an accelerometer to one spot on the outside surface of the ring gave roughly the same statistics exhibited in Table B1 for different spots on the outside surface.

Table B1
Accelerometer Readings E in Air

Reading	$E \alpha v_\xi$ (volts rms)	$\lvert E - E_{av} \rvert$
Outside Surface		
1	0.225	0.016
2	0.257	0.016
3	0.277	0.036
4	0.227	0.014
5	0.214	0.027
6	0.269	0.028
7	0.224	0.017
8	0.259	0.018
9	0.213	0.028
10	0.245	0.004
11	0.250	0.009
12	0.228	0.013
E_{av}	0.241	—
Inside Surface		
1	0.254	0.004
2	0.245	0.005
3	0.230	0.020
4	0.277	0.027
5	0.264	0.014
6	0.240	0.010
7	0.242	0.008
8	0.249	0.001
9	0.230	0.020
10	0.280	0.030
11	0.236	0.014
12	0.252	0.002
E_{av}	0.250	—
Edge Surface		
1	0.039	0.001
2	0.035	0.003
3	0.045	0.007
4	0.049	0.011
5	0.022	0.016
6	0.037	0.001
E_{av}	0.038	—

The individual measurements of velocity are assumed to have an approximately normal distribution about their mean value E_{av}. Therefore σ_{12}, the standard deviation of the mean value E_{av}, of 12 readings is calculated:

$$\sigma_{12} = \frac{1}{12}\sqrt{\sum_{i=1}^{12} (E_i - E_{av})^2} \ .$$

There is approximately a 68% chance that some new mean value of E_{av}, computed from 12 additional readings, will lie within the band $E_{av} \pm \sigma_{12}$. Also calculated is σ, the standard deviation of a single observation (there is a 68% chance that one additional observation will lie within the band $E_{av} \pm \sigma$):

$$\sigma = \sqrt{\frac{1}{12}\sum_{i=1}^{12} (E_i - E_{av})^2} \ .$$

For the outside surface

$$E_{av} = 0.241 \text{ volt rms},$$

$$\sigma_{12} = 0.006 \text{ volt rms},$$

$$\sigma = 0.021 \text{ volt rms}.$$

For the inside surface

$$E_{av} = 0.250 \text{ volt rms},$$

$$\sigma_{12} = 0.005 \text{ volt rms},$$

$$\sigma = 0.016 \text{ volt rms}.$$

For the edge

$$E_{av} = 0.038 \text{ volt rms},$$

$$\sigma_6 = 0.003 \text{ volt rms},$$

$$\sigma = 0.009 \text{ volt rms}.$$

The percent deviation of E_{av} for the outside surface from E_{av} for the inside surface is 3.7%. Since $|v_\xi|$ is directly proportional to E_{av}, the measured deviation in air of the ring outside-surface radial velocity from the ring inside-surface radial velocity was 3.7%. This difference is well within the standard deviations of the mean values; therefore the inside and outside velocities were taken to be equal. Also,

$$\frac{E_{av} \text{ axial}}{E_{av} \text{ radial}} = \frac{|v_y|}{|v_\xi|} = \frac{0.038}{0.246} = 0.15.$$

Thus the axial velocity was 15% of the average radial velocity.

The six accelerometers were epoxied to the ring and suitably coated with Vulcalock and D-202 for underwater velocity measurements. Two were put on the inside surface of the ring, two on the outside surface, and two on the edge. Two of the six accelerometer coatings leaked, rendering the accelerometers useless. The measured output voltages from the other four accelerometers through the charge amplifier when the ring was excited at 6.1 kHz with 200 milliamperes rms current are given in Table B2.

Readings 1, 2, and 3 correspond to an acceleration of 9.7 g peak, and reading 4 corresponds to 1.4 g peak, where $g = 980$ cm/sec^2. The rms velocity of the ring surface at $I =$ 172 milliamperes rms and frequency = 6.1 kHz, which were the operating parameters of the near-field scans, is given by

Table B2
Accelerometer Readings E in Water

Reading	Location	E (volts rms)*
1	Outside surface	0.34
2	Inside surface	0.34
3	Inside surface	0.34
4	Edge surface	0.51

*The reading error is ±0.005 *V*.

$$|v| = \frac{\text{peak acceleration}}{\sqrt{2}\,w} \times \frac{172}{200}.$$

From readings 1, 2, and 3

$$|v_\xi| = \frac{9.7 \times 980}{\sqrt{2} \times 2\pi \times 6100} \times \frac{172}{200} = 0.15 \text{ cm/sec.}$$

From reading 4

$$|v_y| = 0.023 \text{ cm/sec.}$$

The accelerometer measurements of the ring in water confirmed the velocity distribution of the transducer measured in air at the same frequency and comparable drive levels and provided the absolute values of the surface velocity of the ring during the experiment.

For both the air and the water measurements the accelerometer outputs from the inside and outside surfaces of the ring were 180° out of phase; furthermore the accelerometer outputs from the edges were in phase with those from the inside surface. These determinations were consistently valid within the ±6° reading error of the relative phases of two signals on the oscilloscope. The phase results indicated that as the ring expanded (as the inner and outer diameters increased during a typical oscillation), the height of the ring $2L$ simultaneously decreased.

APPENDIX C
ERROR ANALYSIS

THE RECEIVER SYSTEM

The voltage into the receiving system which gave a level of 0 dB at the chart recorder was 94 mV rms. This voltage was read to ±1 mV. All values of pressure magnitude were read directly off a chart recording at the output of the receiving system. The accumulated error in reading the chart and in the stability of the gain of the receiving system was estimated to be ±0.2 dB.

PHASE MEASUREMENTS

Pressure phases were measured by comparing the output of the hydrophone to a reference signal of the same frequency on the chopped-sweep-mode operation function of an oscilloscope. The relative phase on the oscilloscope could be read to only ±6 degrees. Since the signals were pulsed, a more accurate CW-reading phasemeter could not be used. It is hoped that a pulsed phasemeter, which has been purchased for the NRL Tank Facility, will allow improvement in the accuracy of reading phase. There was a net phase shift in the receiver system filter of 40 ±2 degrees at 6.1 kHz. The operating frequency of 6.1 kHz was stable to ±1 Hz.

ALIGNMENT

The hydrophone was aligned relative to the transducer by the electrical-resistance closed-circuit method described in the main text. The precision of this technique was subject to corrosion of the electrical contact points in the environment of chlorinated water; also, the vibrations of the hydrophone and the transducer in the water led to intermittant contact when the probe and transducer were just barely touching. As a result of these sources of error the initial alignment of the hydrophone with respect to a fixed point on the transducer by the use of the electrical-resistance closed-circuit method was known to approximately 0.05 inch in each coordinate direction. The subsequent positions of the hydrophone, during scans, relative to its initial reference location was known to ± 0.02 inch. This latter error is inherent in the automatic scanning and positioning system. During the course of the automatic scans of the hydrophone in the field of the transducer the hydrophone vibrated slightly, but the vibrations were of relatively high frequency and were centered about the accurately determined mean position of the hydrophone.

A misalignment of as much as 0.05 + 0.02 or 0.07 inch corresponded to a phase error at 6.1 kHz of $(0.07/9.74)360^\circ \approx 2.6^\circ$, which is small compared with the phase-measurement

uncertainty of ±6 degrees. The corresponding pressure-amplitude uncertainty at $X = 3.7$ inches and $Y' = 0.06\lambda$ (Fig. 7), where the measured pressure gradient was maximum, was 0.3 dB, which is the same order of magnitude as the ±0.2-dB error in the receiver system.

RING DIMENSIONS

The dimensions of the ring transducer used in this experiment were not completely uniform, because the outside surfaces of the ring were formed in a wooden mold and then smoothed by grinding and sanding. The inner and outer diameters varied ±0.010 inch around the circumference of the ring. The height and thickness of the ring varied ±0.015 inch. The average values of numerous micrometer measurements are represented in Fig. 2.

THE LC-10 HYDROPHONE

The active element in the LC-10 hydrophone is a ceramic cylindrical shell plated on the inside and outside surfaces. It is approximately 1/2 inch long, 1/4 inch in diameter and 0.04 inch thick. The Atlantic Research data sheet on the LC-10 shows the center of the acoustic field of the hydrophone to be on the axis of the hydrophone and 0.38 inch back from the tip of the hydrophone. All pressures measured in this experiment were assumed to have corresponded to the physical position of the center of the acoustic field of the hydrophone. Actually the voltage out of the hydrophone was proportional to the integral of the pressure distribution over the area of the active element. Consequently the assumption in this experiment is that the average of the distributed pressure over the active element was approximately the value of the pressure at its geometric center. Because the center of the acoustic field of the hydrophone was 0.38 inch back from the tip of the hydrophone boot and in addition the electrical-resistance closed-circuit feeler probe protruded 0.08 inch beyond the tip of the hydrophone boot, the closest proximity of the center of the hydrophone's acoustic field to the transducer was 0.38 + 0.08 = 0.46 inch. This corresponds to 0.047λ at 6.1 kHz (Fig. 12). Thus, the values of pressure magnitude $|p|_c$, phase α_c, pressure-magnitude gradient $(\Delta|p|/\Delta\xi)_c$, and phase gradient $(\Delta\alpha/\Delta\xi)_c$ evaluated at the surface of the transducer were actually extrapolated from values measured very near the surface.

ELECTRICAL MEASUREMENTS

The voltage and current into the ring were measured on the same meter to 2 parts in 100. The real part of the electrical impedance of the ring was read directly to ±0.2 ohm. Therefore the error in the calculated average electrical power dissipated into the ring is less than 8 parts in 100.

VELOCITY DETERMINATION

To calculate the velocity of the ring surface, the real acoustic power radiated, and the radiation impedance of the ring from the near-field pressure-magnitude and phase measurements, a value of the pressure magnitude, the pressure phase, the slope of the pressure

magnitude versus radial distance, and the slope of the pressure phase versus radial distance were extrapolated to the surface of the ring. The error in α_c, which was extrapolated from the extension of the curve in Fig. 11, is estimated to be less than ±6 degrees = ±0.1 radian. The error in $|p|_c$, which was extrapolated from the extension of the curve in Fig. 13, is estimated to be less than $\pm 0.05 p_0$. The error in $(\Delta\alpha/\Delta\xi)_c$ extrapolated to the surface of the ring in Fig. 11 is estimated to be less than ±0.02 radian/cm. The error in $(\Delta|p|/\Delta\xi)_c$ extrapolated to the surface of the ring in Fig. 13 is estimated to be less than $\pm 1.6 \times 10^3$ dynes/cm^3. The values of $|p|_c$ and $(\Delta|p|/\Delta\xi)_c$ extracted from Fig. 13 are more subject to error than the values of α_c and $(\Delta\alpha/\Delta\xi)_c$ extracted from Fig. 11, because the curve in Fig. 13 is much steeper near the surface of the ring than the curve in Fig. 11. Consequently its intercept and slope are much more sensitive to the coordinates of the few points closest to the ring surface. The rms error in $|v_\xi|$, calculated from the magnitudes and errors of the coordinates and slopes of the curves in Figs. 11 and 13, is 0.05 cm/sec. The corresponding error in radiated power is less than 0.05 watt. Since the calculated radiation impedance is a complex number, there are errors associated with the real and the imaginary parts.

The error in Z is given in

$$Z + \Delta Z = \frac{[(15 \pm 5) - (17 \pm 6)j] \times 10^5}{(0.17 \pm 0.05)^2} \text{ dyne sec/cm.}$$

The following is a list of the important derived parameters and their errors used in the analysis:

$$|p|_c = 0.78 p_0 \pm 0.05 p_0$$

$$\alpha_c = -\frac{10\pi}{180} \pm \frac{6\pi}{180} \text{ radians,}$$

$$\left(\frac{\Delta|p|}{\Delta\xi}\right)_c = -5.0 \times 10^3 \pm 1.6 \times 10^3 \text{ dynes/cm}^3,$$

$$\left(\frac{\Delta\alpha}{\Delta\xi}\right)_c = 0.14 \pm 0.02 \text{ rad/sec,}$$

$$|v_\xi| = 0.17 \pm 0.05 \text{ cm/sec,}$$

$$P_a = 0.15 \pm 0.05 \text{ watt.}$$

EDGE RADIATION

The contribution of the edges of the ring to the total radiation impedance and radiated power was neglected in the analysis. The justification for this omission is seen in the following argument. First, the ratio of the edge area to the total inside and outside circumferential area is 0.33. Second, the ratio of the pressure in the medium at the edge to the average pressure in the medium at the inside and outside circumferential surfaces of the ring is 0.63.

Third, the ratio of the magnitude of the normal velocity to the edge surface (the axial velocity of the ring), which was measured directly by accelerometers, to the ring radial velocity is 0.15. Since the radiation impedance is proportional to the product of these three factors, the contribution of the edge loading to the radiation impedance of the ring is 0.33 x 0.63 x 0.15 = 0.03 or 3%. The contribution of the edge radiation to radiated acoustic power is also only 3% of the radial surface contributions.

APPENDIX D
A TABULATION OF MEASURED NEAR-FIELD PRESSURE MAGNITUDES AND PHASES AND THE CALCULATION OF THE TRANSMITTING EFFICIENCY AND RADIATION IMPEDANCE

The values of $|p|_i$ and α_i corresponding to the 46 circumferential strips into which the inside and outside surface of the ring was divided are tabulated in Table D1. These values were not actually measured at the surface but (as discussed in Appendix C in the section "The LC-10 Hydrophone") were extrapolated from values measured very near the surface. The strip centered at ξ = outer radius and $y = 0$ is strip 12. The magnitude $|p|_c$ of the complex rms pressure at strip 12, is $0.78p_0$, where $p_0 = 4.0 \times 10^4$ dynes/cm^2. The corresponding phase α_c of the pressure relative to the ring driving voltage is $-10°$. From Fig. 11, $(\Delta\alpha/\Delta\xi)_c = 0.14$ rad/cm. From Fig. 13, $(\Delta|p|/\Delta\xi)_c = -5.0 \times 10^3$ dynes/cm. Since $\alpha_i = \alpha_c + \epsilon_i$, then $\epsilon_i = \alpha_i - \alpha_c$. As examples the values in Table D1 give

$$\epsilon_1 = \alpha_1 - \alpha_c = -19° - (-10°) = -9°$$

and

$$\epsilon_{24} = \alpha_{24} - \alpha_c = -190° - (-10°) = -180°.$$

Thus the remaining values needed in calculating P_a using Eq. (7) are

$$\sum_{i=1}^{23} |p|_i \cos \epsilon_i = [0.50 \cos 9° + (0.55 + 0.57) \cos 3° + (0.61 + 0.64 + 0.66 + 0.68 + 0.70 + 0.72 + 0.76 + 0.77 + 0.78 + 0.77 + 0.76 + 0.74 + 0.72 + 0.71 + 0.68 + 0.66 + 0.62) \cos 0° + 0.58 \cos 3° + 0.52 \cos 9° + 0.47 \cos 15°] \times 4 \times 10^4 \text{ dynes/cm}^2$$

(outside surface strips)

$$= 15 \times 4 \times 10^4 \text{ dynes/cm}^2,$$

$$\sum_{i=1}^{23} |p|_i \sin \epsilon_i = -[0.50 \sin 9° + (0.55 + 0.57) \sin 3° + 0.58 \sin 3° + 0.52 \sin 9° + 0.47 \sin 15°] \times 4 \times 10^4 \text{ dynes/cm}^2$$

(outside)

$$= -0.37 \times 4 \times 10^4 \text{ dynes/cm}^2,$$

$$\sum_{\substack{i=24 \\ \text{(inside)}}}^{46} |p|_i \cos \epsilon_i = [(0.55 + 0.61 + 0.68 + 0.73 + 0.77 + 0.82 + 0.84 + 0.86 + 0.91 + 0.92 + 0.92 + 0.93 + 0.93 + 0.93 + 0.93 + 0.92 + 0.90 + 0.84 + 0.80 + 0.73 + 0.65 + 0.58 + 0.51) \cos 180^\circ] \times 4 \times 10^4 \text{ dynes/cm}^2$$

$$= -18 \times 4 \times 10^4 \text{ dynes/cm}^2,$$

$$\sum_{\substack{i=24 \\ \text{(inside)}}}^{46} |p|_i \sin \epsilon_i = 0.$$

Table D1
Measured Pressure Magnitude and Phase Extrapolated to the Ring's Surface

Outside Circumferential Strip	$\frac{\lvert p\rvert_i}{p_0}$	α_i (degrees)
1	0.50	-19
2	0.55	-13
3	0.57	-13
4	0.61	-10
5	0.64	-10
6	0.66	-10
7	0.68	-10
8	0.70	-10
9	0.72	-10
10	0.76	-10
11	0.77	-10
12*	0.78	-10
13	0.77	-10
14	0.76	-10
15	0.74	-10
16	0.72	-10
17	0.71	-10
18	0.68	-10
19	0.66	-10
20	0.62	-10
21	0.58	-13
22	0.52	-19
23	0.47	-25

Inside Circumferential Strip	$\frac{\lvert p\rvert_i}{p_0}$	α_i (degrees)
24	0.55	-190
25	0.61	-190
26	0.68	-190
27	0.73	-190
28	0.77	-190
29	0.82	-190
30	0.84	-190
31	0.86	-190
32	0.91	-190
33	0.92	-190
34	0.92	-190
35	0.93	-190
36	0.93	-190
37	0.93	-190
38	0.93	-190
39	0.92	-190
40	0.90	-190
41	0.84	-190
42	0.80	-190
43	0.73	-190
44	0.65	-190
45	0.58	-190
46	0.51	-190

*$|p|_{12} = |p|_c$ and $\alpha_{12} = \alpha_c$.

Substitution of these various values in Eq. (7) yields

$$P_a = \frac{4 \times 10^4}{2\pi \times 6100 \times 1} \{[15 \times 0.78 \times 4 \times 10^4 \times 0.14 - (-0.37)(-5.0 \times 10^3)]6.53$$

$$-[-18 \times 0.78 \times 4 \times 10^4 \times 0.14]5.30\} \frac{\pi}{12} \times (2.54)^2$$

$$= 15 \times 10^5 \text{ ergs/sec} = 0.15 \text{ watt.}$$

To calculate the radiation impedance Z as defined by Eq. (8), a summation must be performed over both the real and the imaginary parts of pv_ξ^*:

$$Z|v|^2 = \int_S pv_\xi^* \, dS = \text{Re}\left(\int_S pv_\xi^* \, dS\right) + j \, \text{Im}\left(\int_S pv_\xi^* \, dS\right). \tag{D1}$$

The real part of $\int_S pv_\xi^* \, dS$ is calculated by Eq. (7) and is identically equal to P_a:

$$P_a = \text{Re}\left(\int_S pv_\xi^* \, dS\right) = 15 \times 10^5 \text{ ergs/sec.}$$

Also,

$$|v|^2 = 0.029 \text{ (cm/sec)}^2.$$

Thus the determination of Z depends on the evaluation of Im $(\int_S pv_\xi^* \, dS)$:

$$\text{Im}\left(\int_S pv_\xi^* \, dS\right) = \text{Im}\left(\underbrace{\sum_{i=1}^{23} p_i v_\xi^* \Delta S_i}_{\text{(outside)}} + \underbrace{\sum_{i=24}^{46} p_i v_\xi^* \Delta S_i}_{\text{(inside)}}\right). \tag{D2}$$

For the outside surface

$$\text{Im}\,(p_i v_\xi^*) = \text{Im}\left\{ |p|_i \frac{e^{j\epsilon_i}}{w\rho}\left[j\left(\frac{d|p|}{d\xi}\right)_c + |p|_c\left(\frac{d\alpha}{d\xi}\right)_c\right]\right\}$$

$$= \frac{|p|_i}{w\rho}\left[|p|_c\left(\frac{d\alpha}{d\xi}\right)_c \sin\epsilon_i + \left(\frac{d|p|}{d\xi}\right)_c \cos\epsilon_i\right].$$

Similarly for the inside surface

$$\text{Im}\,(p_i v_\xi^*) = \frac{-|p|_i}{w\rho}\left[|p|_c\left(\frac{d\alpha}{d\xi}\right)_c \sin\epsilon_i + \left(\frac{d|p|}{d\xi}\right)_c \cos\epsilon_i\right].$$

Substituting these in Eq. (D2) gives

$$\mathrm{Im}\left(\int_S pv_\xi^* \, dS\right) = \frac{1}{w\rho}\left\{ \sum_{\substack{i=1 \\ \text{(outside)}}}^{23} |p|_i \left[|p|_c \left(\frac{d\alpha}{d\xi}\right)_c \sin\epsilon_i + \left(\frac{d|p|}{d\xi}\right)_c \cos\epsilon_i\right]\Delta S_i \right.$$

$$\left. - \sum_{\substack{i=24 \\ \text{(inside)}}}^{46} |p|_i \left[|p|_c \left(\frac{d\alpha}{d\xi}\right)_c \sin\epsilon_i + \left(\frac{d|p|}{d\xi}\right)_c \cos\epsilon_i\right]\Delta S_i \right\}$$

$$= \frac{4 \times 10^4}{2\pi \times 6100 \times 1}\left\{[-0.37 \times 0.78 \times 4 \times 10^4 \times 0.14 + (-5.0 \times 10^3 \times 15)]6.53 - [0 - 18 \times (-0.50 \times 10^4)]5.30\right\}\frac{\pi}{12} \times (2.54)^2$$

$$= -17 \times 10^5 \text{ ergs/sec.}$$

Substituting this in Eq. (D1) yields

$$Z = \frac{15 \times 10^5 - j \times 17 \times 10^5}{0.029}$$

$$= (52 - 59j) \times 10^6 \text{ dyne sec/cm.}$$

Security Classification

UNCLASSIFIED

DOCUMENT CONTROL DATA - R & D

(Security classification of title, body of abstract and indexing annotation must be entered when the overall report is classified)

1. ORIGINATING ACTIVITY *(Corporate author)*

Naval Research Laboratory
Washington, D.C. 20390

2a. REPORT SECURITY CLASSIFICATION

Unclassified

2b. GROUP

3. REPORT TITLE

Acoustic Near-Field Measurements of a Free-Flooded Magnetostrictive Ring

4. DESCRIPTIVE NOTES *(Type of report and inclusive dates)*

An interim report on a continuing NRL Problem

5. AUTHOR(S) *(First name, middle initial, last name)*

Joel A. Sinsky

6. REPORT DATE	7a. TOTAL NO. OF PAGES	7b. NO. OF REFS
December 30, 1971	40	6

8a. CONTRACT OR GRANT NO.	9a. ORIGINATOR'S REPORT NUMBER(S)
NRL Problem S02-19	
b. PROJECT NO. RF 05-121-402-6200	NRL Report 7328
c.	9b. OTHER REPORT NO(S) *(Any other numbers that may be assigned this report)*
d.	

10. DISTRIBUTION STATEMENT

Approved for public release; distribution unlimited

11. SUPPLEMENTARY NOTES	12. SPONSORING MILITARY ACTIVITY
	Department of the Navy Office of Naval Research Arlington, Va. 22217

13. ABSTRACT

Precision acoustic near-field pressure magnitude and phase measurements have been made of radially oscillating free-flooded cylindrical ring. The measurements demonstrate the potential of the NRL Acoustic Research Tank Facility for careful determination of near-field pressure magnitude and phase. Various pressure profiles and phase profiles were plotted. Besides demonstrating results possible with the Tank Facility the profiles were used in deriving dynamic properties of the ring. The transmitting efficiency, surface velocity, and radiation impedance of the ring were derived from the near-field data and were independently confirmed by other methods. Further analysis than that presented here can predict the acoustic interaction through the medium among many rings in an array.

DD FORM 1 NOV 65 1473 (PAGE 1)

S/N 0101-807-6801

Security Classification

14. KEY WORDS	LINK A		LINK B		LINK C	
	ROLE	WT	ROLE	WT	ROLE	WT
Acoustic fields						
Magnetostriction transducers						
Free-flooded ring						
Acoustic measurement						
Acoustic measuring instruments						
Sound pressure						
Phase measurement						
Underwater sound sources						
Near Field						